GA–A24204

TRANSPORT OF ELM ENERGY AND PARTICLES INTO THE SOL AND DIVERTOR OF DIII–D

by
A.W. LEONARD, T.H. OSBORNE, M.E. FENSTERMACHER,
R.J. GROEBNER, M. GROTH, C.J. LASNIER, M.A. MAHDAVI,
T.W. PETRIE, P.B. SNYDER, J.G. WATKINS, and L. ZENG

NOVEMBER 2002

DISCLAIMER

GA–A24204

TRANSPORT OF ELM ENERGY AND PARTICLES INTO THE SOL AND DIVERTOR OF DIII–D

by
A.W. LEONARD, T.H. OSBORNE, M.E. FENSTERMACHER,*
R.J. GROEBNER, M. GROTH,* C.J. LASNIER,* M.A. MAHDAVI,
T.W. PETRIE, P.B. SNYDER, J.G. WATKINS,† and L. ZENG‡

This is a preprint of an invited paper to be presented at the 44th Annual Meeting of the Division of Plasma Physics, Orlando, Florida, November 11–15, 2002, and to be published in *Phys. Plasmas.*

*Lawrence Livermore National Laboratory, Livermore, California.
†Sandia National Laboratories, Albuquerque, New Mexico.
‡University of California, Los Angeles, Califoronia.

Work supported by
the U.S. Department of Energy under
Contract Nos. DE-AC03-99ER54463, W-7405-ENG-48,
and DE-AC04-94AL85000 and Grant No. DE-FG03-01ER54145

GENERAL ATOMICS PROJECT 30033
NOVEMBER 2002

ABSTRACT

The reduction in size of Type I edge localized modes (ELMs) with increasing density is explored in DIII-D [J.L. Luxon, Nucl. Fusion **42**, 614 (2002)] for the purpose of studying the underlying transport of ELM energy. The separate convective and conductive transport of energy due to an ELM is determined by Thomson scattering measurements of electron density and temperature in the pedestal. The conductive transport from the pedestal during an ELM decreases with increasing density, while the convective transport remains nearly constant. The scaling of the ELM energy loss is compared with an edge stability model. The role of the divertor sheath in limiting energy loss from the pedestal during an ELM is explored. Evidence of outward radial transport to the midplane wall during an ELM is also presented.

I. INTRODUCTION

Energy deposition on the divertor target plates due to edge localized modes (ELMs) is a significant concern for the next generation of burning plasma tokamak experiments (BPX) such as ITER [1,2]. While a robust H-mode edge pedestal is needed for adequate confinement, steady-state H-mode operation typically results in periodic relaxation of the edge barrier through ELMs. The transient energy and particles released from the pedestal into the scrape-off-layer (SOL) due to ELMs can potentially cause unacceptable erosion of the divertor target if the heat pulse causes the surface temperature to rise above the ablation, or melting point, of the target material. This concern has motivated a search for small-ELM or no-ELM regimes. Several such regimes have been identified and include QH-mode in DIII-D [3,4], "grassy" ELMs in JT-60U [5], Type II ELMs in ASDEX-Upgrade [6] and enhanced D-alpha (EDA) mode in Alcator-C-Mod [7,8]. However, it is unclear if any of these regimes will be accessible to, or compatible with, a BPX device. Therefore current BPX designs remain based upon the common, or Type I, ELM regime that is robustly observed in all large divertor tokamaks. It is therefore important to understand the underlying physics of Type I ELMs and predict how their characteristics will scale from present tokamaks to a larger BPX scale device.

The surface temperature rise of the divertor plate due to a transient heat pulse is roughly proportional to the energy density deposited, divided by the square root of the heat pulse duration. For the plasma-facing materials under consideration, *i.e.,* carbon and tungsten, this threshold is expected to be ~40 $MJm^{-2}s^{-1/2}$. The potential for ablation can then be assessed if the following parameters can be predicted for future devices: (1) the energy lost from the main plasma due to an ELM, (2) the fraction of ELM energy falling on the divertor target, (3) the area of the ELM deposition on the divertor target and (4) the duration of the heat flux deposition. Considering data from present devices, it is estimated that in order to avoid material ablation in ITER, the ELM energy lost from the main plasma should be less than 5%-10% of the pedestal energy [9], where the pedestal energy is given by the plasma volume times the total pressure at the top of the edge pedestal.

The energy lost from the main plasma, the first parameter listed above, has been observed in current devices [10-12] to vary from >20% of the pedestal energy at low density to <5% at high density. A better physical understanding of this density dependence is needed to improve the reliability of extrapolating these results in present tokamaks to future larger devices. The purpose of this study is to examine the scaling of ELM energy on DIII-D, with the goal of determining which processes are responsible for the dependence on density. The data is examined in the context of two possible mechanisms that could be controlling the ELM energy loss. The first process examined is the MHD stability of the edge pedestal. A comparison is made between the width of unstable region in the edge and the ELM size. The other process considered is that the sheath at the divertor target is limiting the heat flow along field lines out of the pedestal to the divertor during the ELM instability. This limitation could become even stronger at high density.

In Section II the density dependence of the ELM energy lost from the pedestal, as measured by Thomson scattering, is examined for the conducted and convected components separately. The density dependence of these components are then compared with an edge MHD stability model as calculated by the ELITE code. In Section III the transport of ELM energy along field lines from the midplane in the SOL and divertor is examined. No evidence for the divertor target sheath limiting the loss of pedestal energy at an ELM is found. Evidence of fast radial transport in the SOL during an ELM is also presented. In Section IV the implications of the experimental observations are discussed.

II. ELM ENERGY LOST FROM PEDESTAL

The energy lost from the core plasma due to an ELM can be measured on DIII-D by use of the Thomson scattering diagnostic, Fig. 1, [13]. A fast measurement, $< 1\ \mu s$, of the radial profile of T_e and n_e is produced every ~12 ms by Thomson scattering. To determine the effect of an ELM on the density and temperature, the individual profiles are collected during steady-state ELMing conditions and then re-ordered in time with respect to the nearest ELM. A D_α channel with a vertical view of the lower outer wall outside of the divertor is used as the reference time for each ELM. This channel avoids the slower evolution of divertor recycling which can produce a D_α peak with a significant delay from the ELM event. An example of the time dependence this re-ordering produces is shown in Fig. 2 for a location near the top of the pedestal. Both density and temperature show a gradual increase up to the ELM, a sharp drop at the ELM, and then a gradual recovery. In order to determine the value just before, and just after, the ELM the pre-ELM and post-ELM values are separately fit with a linear function. The intersection of these fits with the time of the ELM determines the pre-ELM and post-ELM values. Fitting the slower evolution of the profiles separately before and after an ELM, typically ~10 ms, helps to overcome any uncertainty in the exact timing of the ELM transport event, up to 100–200 μs. The intersection values from each measurement location can then be combined into a pre-ELM and post-ELM profile as shown in Fig. 3.

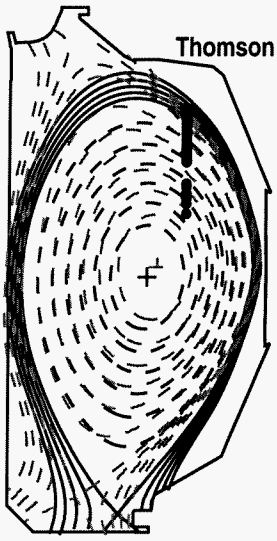

FIG. 1. The magnetic equilibria for the discharges of this study. The dashed lines show the high triangularity configuration, $\delta \sim 0.4$. Also shown are the Thomson scattering measurement locations.

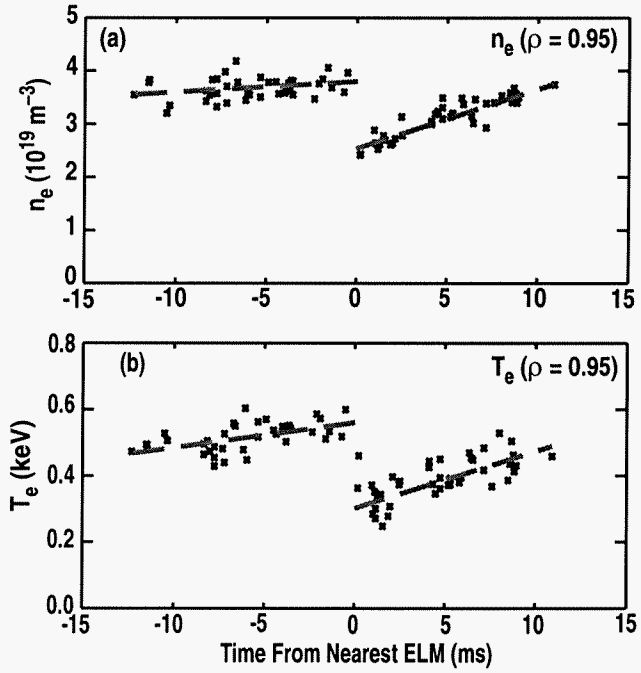

FIG. 2. Fitting of the time history of Thomson measurements at $\rho = 0.95$ reordered with respect to the nearest ELM. Both (a) density and (b) temperature are fit. The pre-ELM and post-ELM values are given at $t = 0$.

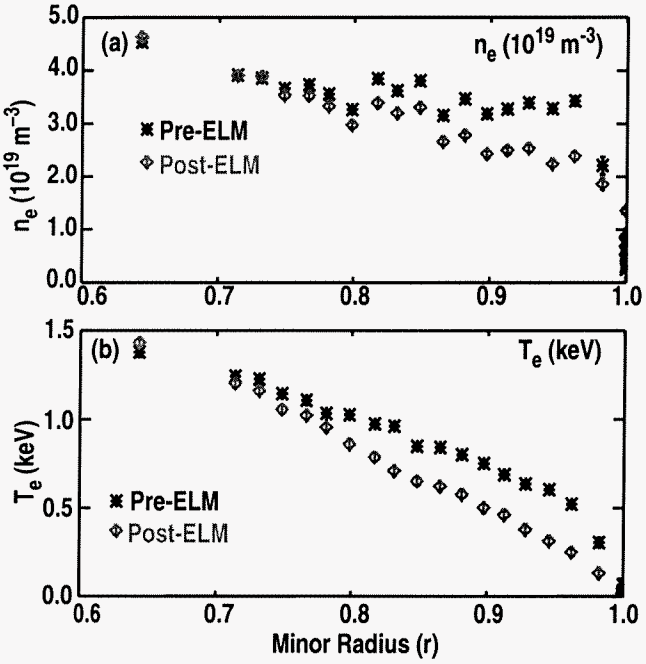

FIG. 3. Radial profiles of (a) n_e and (b) T_e fit before and after an ELM.

The difference between the pre-ELM and post-ELM profiles can be integrated to determine the electron energy lost at an ELM. As discussed above the ELM energy is split into its convective and conductive parts in order to study the underlying transport processes. The convected electron energy is given by integrating $3/2 \langle T_e \rangle \Delta n_e$ over the plasma volume, where $\langle T_e \rangle$ is the average of the pre-ELM and post-ELM T_e values and Δn_e is the difference between pre-ELM and post-ELM density. The convected energy term represents plasma that is displaced from the pedestal into the SOL. A process such as $E \times B$ driven transport from the ELM instability could result in such an energy loss. Similarly the conducted electron energy is given by integrating $3/2 \langle n_e \rangle \Delta T_e$. This loss term represents a cooling of the pedestal, and arises from temperature-gradient driven transport between the pedestal and the colder plasma of the SOL and divertor. Transport along open field lines from the pedestal to the SOL and divertor due to the ELM instability is one mechanism that would allow the exchange of hotter pedestal plasma with cooler divertor plasma.

The ELM energy lost by ions should also be considered since the Thomson analysis is only a measurement of electron energy. For the ion convected energy an estimate is needed for both Δn_i and T_i. A Z_{eff} of ~1.8 was measured in several discharges, implying

an ion density 85% of the electron density if carbon is the dominant impurity. Off-setting this ion dilution are typical measurements of ion temperature somewhat higher than the electron temperature in the pedestal steep gradient region. For these reasons the convected ion energy at an ELM will be assumed to be equal to that of the electrons. For the ion conducted energy a measurement of ΔT_i is needed. To determine ΔT_i at an ELM the charge-exchange-recombination (CER) diagnostic was operated with a fast integration time of 0.5 ms for several discharges. Initial analysis of the data indicates a discernible drop in T_i at an ELM, but ≤25% of that for the electrons. Because of this small value, some additional uncertainty in the interpretation of the fast T_i measurements and the limited data set the ion conducted energy will be ignored for this study. Further experiments and analysis will be required to better determine the relationship between ΔT_i and ΔTe at an ELM. These approximations described above will later be shown to give reasonable agreement when compared to ELM energy obtained from fast magnetic equilibrium reconstruction.

The analysis described above was used for a series of discharges in a low triangularity, $\delta \approx 0$, lower single-null (LSN) configuration as shown by the solid lines in Fig. 1. Also several discharges were obtained at a higher triangularity, $\delta \approx 0.4$, to assess the dependence on triangularity. The low triangularity discharges were produced with variations in plasma current of 0.8–2.0 MA in a toroidal field of 1.4–2.1 T for a variation in safety factor q_{95} of 2.5–6.0. Divertor pumping in all configurations allowed for a range in pedestal density of 2–13×10^{19} m^{-3} corresponding to a normalized pedestal density range of 0.2–0.9 times the Greenwald density, $n_{GW}\left(10^{20}\,\mathrm{m}^{-3}\right) = I_p(\mathrm{MA})/\left[\pi a^2(\mathrm{m})\right]$.

The normalized convected ELM energy from this series of density scans is plotted in Fig. 4(a) versus the normalized pedestal density, n_{ped}/n_{GW}. The ELM energies in these plots are normalized by the pedestal energy, three times the pedestal electron pressure times the plasma volume, to account for any variations in pedestal pressure. This normalization assumes $T_i \approx T_e$. As reported earlier in Ref. [13], while there is significant scatter, the normalized convected ELM energy remains constant versus density up to $n_{e,ped}/n_{GW} \sim 0.65$ after which the ELMs become smaller. This trend is represented by a dashed line to guide the eye. There is also no obvious q_{95} dependence among the

different cases. It should also be noted that the higher current and higher triangularity cases have about a factor of 2 higher pressure pedestal, but the ELM energy remains a constant fraction of the pedestal energy. For the energy convected, this is equivalent to losing a fixed fraction of the pedestal density at an ELM for all conditions.

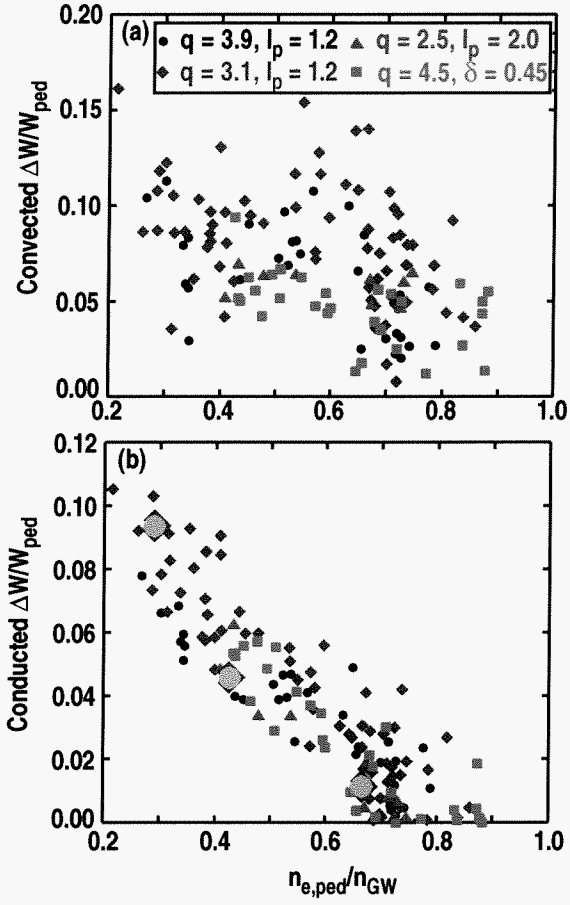

FIG. 4. (a) The normalized convected ELM energy as measured by the Thomson profile versus the pedestal density normalized by the Greenwald parameter, $n_{e,ped}/n_{GW}$ shows no clear density dependence. (b) The normalized conducted ELM energy versus the normalized pedestal density shows a strong decreasing trend with increasing density. Three cases, low medium and high density, for $q = 3.1$ are highlighted for stability analysis.

The conducted ELM energy, in contrast, shows a clear decrease with density. The conducted ELM energy is highest at low density and decreases with density to near zero at $n_{e,ped}/n_{GW} \sim 0.7$. At high density the scatter is due in part to a degradation in the pedestal pressure. This results in small ELMs near the measurement sensitivity and a large scatter in the relative ELM size. All four cases follow the same trend within the data

scatter. This implies a similar density dependence for the conducted energy regardless of q_{95}, plasma current, or triangularity variation of this data.

At high density, $n_{e,ped}/n_{GW} \geq 0.65$ the Thomson measurement technique becomes more difficult and produces a larger scatter. This arises in a large part due to irregular ELM behavior with many small peaks in D_α between larger ones. For this analysis at high density only the largest D_α peaks were used as ELM timing references for the Thomson reordering. This criterion exhibited the largest perturbation to the density and temperature profiles though the scatter in the perturbed profiles, particularly the density, remained large.

To confirm these trends and cross-check the Thomson analysis, the total ELM energy was obtained for a different series of discharges by equilibrium reconstruction from fast magnetic signals that produced the total plasma stored energy every 0.5 ms. This data is plotted in Fig. 5 with the trends from Fig. 4 overlaid. The ELM energy from fast magnetics shows a clear decrease with increasing density that is similar over a range of average triangularity of 0.0–0.4. The magnitude of ELM energy measured by the magnetic methods is in reasonable agreement with results of the Thomson analysis technique.

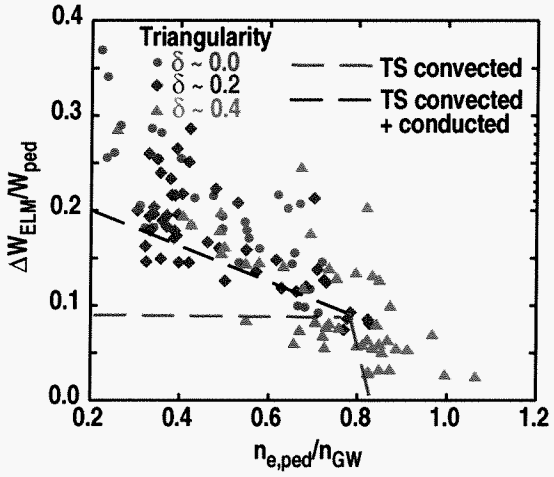

FIG. 5. Normalized ELM energy measured by fast magnetic equilibrium reconstruction for a series of discharges with varying triangularity. Overlaid on the data is the convected and conducted ELM energy trends from Fig. 4.

In order to determine if edge MHD stability can explain the decrease in conducted ELM energy with increasing density and to highlight what parameters are responsible for it, three cases of a density scan in a single configuration are examined. These cases are highlighted in Fig. 4(b). The ELM instability for this analysis is modeled as a coupled peeling-ballooning mode that is driven by current and pressure gradients in the pedestal [14]. The growth rates and eigenmode structures for a wide range of toroidal and poloidal mode numbers is calculated by the ELITE code [15] using the measured pressure profile. The edge current density profile used in the analysis is calculated from a collisional bootstrap current model [16] with the measured electron and ion temperature and density profiles.

The ELITE edge stability analysis was carried out for the density points of $n_{e,ped}/n_{GW}$ ~ 0.30, 0.46 and 0.65 at q_{95} ~ 3.1 for $I_p = 1.2$ MA and $B_T = 1.5$ T. The measured edge pressure profiles for this density scan is shown in Fig. 6(a). The pressure profile is obtained from Thomson scattering measurements of the electron density and temperature, and charge-exchange-recombination (CER) spectroscopy measurements for the ion density and temperature. An important aspect of the measured pressure profile is that the steep gradient region is much narrower at high density. Also the calculated edge bootstrap current decreases at higher density, shown in Fig. 6(b), due to the pedestal neoclassical electron collisionality[16], $\nu_e^* = 6.9\times10^{-18}\left(qRn_eZ\ln\Lambda_e/T_e^2\varepsilon^{3/2}\right)$, increasing from 0.8 at low density, $n_{e,ped}\sim3\times10^{19}$, $T_{e,ped}\sim900$ eV, to 15.0 at high density, $n_{e,ped}\sim8\times10^{19}$, $T_{e,ped}\sim200$ eV. Future work is planned to measure the edge current and validate the bootstrap current model [17].

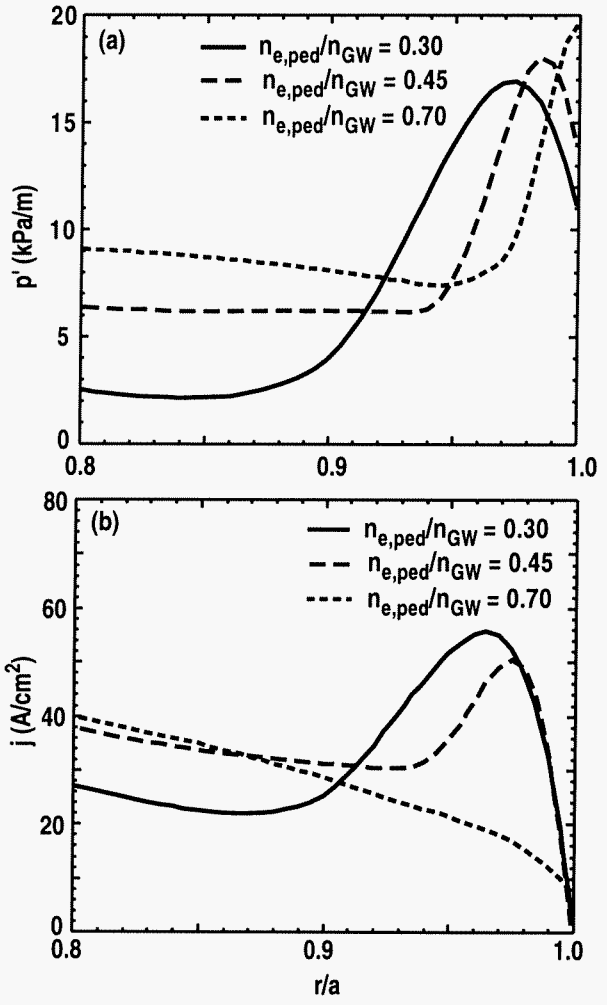

FIG. 6. (a) Edge pressure profiles for densities of $n_{e,ped}/n_{GW}$ ~ 0.30, 0.46 and 0.65 are determined by measurements of electron density and temperature from Thomson scattering and ion density and temperature from CER. (b) The edge current profile is calculated from a collisional bootstrap model using the measured density and temperature profiles.

The growth rates of eigenmodes calculated by ELITE from the profiles of Fig. 6 are summarized in Fig. 7. The most unstable mode increases from $n \sim 20$ at low density to $n \sim 40$ at medium density and finally $n \sim 65$ at high density. The growth rates of Fig. 7(a) are normalized by the toroidal mode number and Alfvén frequency to account for the diamagnetic stabilization effect. The envelope of eigenmodes for all of the poloidal mode numbers associated with the most unstable toroidal mode is shown in Fig. 7(b). At low density the instability affects the outer 6% of the minor radius. This region of instability decreases at higher density until it affects only the outer 2%. The changes to ELM stability with density arise from both the reduced bootstrap current and

narrower pressure gradient at high density. At low density the edge bootstrap current stabilizes the higher n modes which allows the lower n modes to dominate the instability as the edge pressure gradient builds. At high density, and collisionality, the bootstrap current is suppressed and the higher n modes are no longer stabilized and become dominant before the lower n modes can grow. The second effect is that the steep pressure gradient becomes narrower at high density. For higher n modes, or short wavelength, the instability profile becomes closely tied to the pressure gradient, resulting in a narrow eigenmode. This is in contrast to an earlier DIII-D study [15] where the eigenmode structure can extend significantly inside the high gradient region when low toroidal mode numbers, or long wavelength modes, dominate.

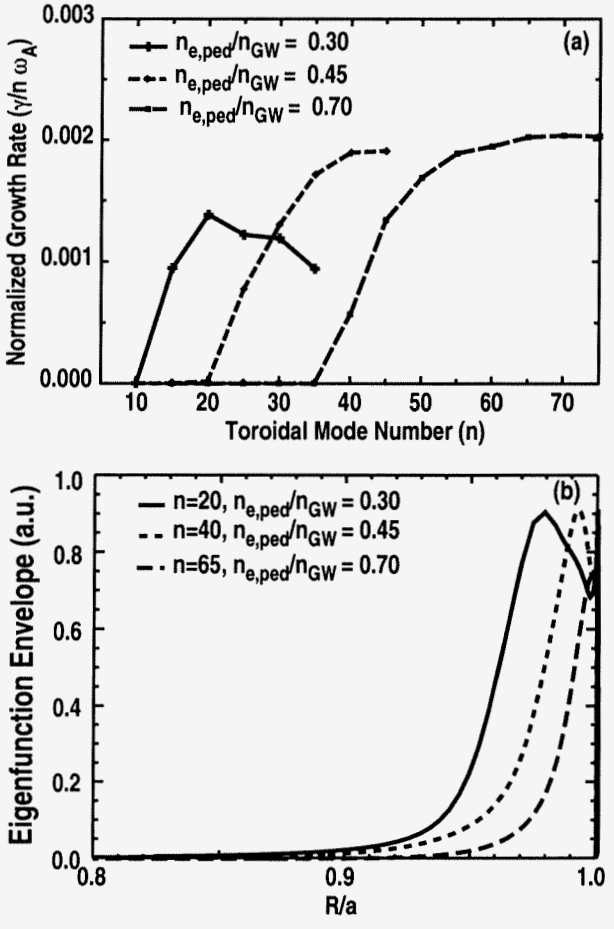

FIG. 7. (a) The normalized growth rate of the peeling-ballooning mode versus toroidal mode number for low, medium and high density, $n_{e,ped}/n_{GW}$ ~ 0.30, 0.46 and 0.65. The growth rate is normalized by the toroidal mode number and the Alfvén frequency to account for diamagnetic stabilization. The instability growth rates are calculated by ELITE using measured edge profiles of Fig 6. (b) The radial eigenmode profile as calculated by ELITE for low, medium and high density.

A basic model of ELM transport in the pedestal arises from the linear MHD stability model described above. Once the peeling-ballooning modes become unstable they grow until they overlap in the edge region. The overlap results in a stochastic magnetic field structure in the pedestal that allows parallel transport to carry energy and particles into the SOL and eventually the divertor. The parallel heat conduction from the pedestal into the SOL can be very large at the observed high pedestal temperatures. It should be noted that the region of perturbation in Fig. 3 is wider than both the steep gradient region and the predicted eigenmode width. This is again in contrast to earlier DIII-D ELM stability analysis [15]. This indicates that there may not be a direct correspondence between the eigenmode width and the affected region. In the previous analysis the eigenmodes of low toroidal mode number ELMs extended far inside the steep gradient. The resulting large ELMs produced a perturbation profile similar in width to the predicted eigenmodes. For the data presented here the unstable modes are much more localized to the edge. The resulting instability though, might evolve into a perturbation profile different from the mode at onset by inward cascading or other nonlinear effects. A narrower drive to the instability, though, should still be expected to lead to a smaller perturbation. A higher mode number could also contribute to a reduction in conducted transport if the modes saturate, or overlap, at a lower amplitude. This would lead to less magnetic diffusion in the resulting stochastic pedestal and less transport. Additional theoretical work will be required to further assess the relationship between the unstable mode characteristics and the resulting transport.

The above stability analysis and correlation of small ELMs with a narrow eigenmode at high mode number is consistent with the scaling of the conducted ELM energy shown in Fig. 4(b). The conducted electron energy is large at low density and decreases as the density is raised. The stability analysis, would indicate this arises from two effects. The first is a loss of edge bootstrap current due to high collisionality at high density. A similar correlation with collisionality has been observed JET [11] and across other tokamaks [12]. But the stability analysis also indicates that other pedestal characteristics, such as the pedestal width, may also play an important role in setting the ELM size. Careful experiments and modeling will be needed to isolate the importance and scaling of

these effects separately before an extrapolation to future larger tokamaks can reliably be made.

The ELM convected energy, however, does not appear to result from the same process of ergodization of the plasma edge. At the temperature of the pedestal, parallel convection of energy should be much less than conduction. This is in contrast to the similar levels of energy transport observed in Fig. 4. Also convection which should proceed at the ion sound speed does not exhibit the density, or temperature, dependence observed for conduction. An accurate description of ELM convected transport awaits further theoretical and experimental advances.

III. SOL AND DIVERTOR RESPONSE TO ELM FLUX

SOL transport processes might also play a role in the magnitude and scaling of energy lost from the pedestal at an ELM. Previous experimental data and theoretical modeling indicate that the ELM instability transport from the pedestal occurs at the low field, or outer midplane, side of the plasma surface [18]. Here we examine ELM transport from the outer midplane SOL into the divertor with DIII-D data in the context of a simple argument that suggests that parallel transport of ELM energy in the SOL is limited to the ion sound speed [2,19,20]. At the ELM instability particles and energy are transported across the outer midplane separatrix into the SOL. Fast parallel electron transport should quickly carry the heat to the divertor plasma within 10-20 μs for DIII-D parameters. The ions and their energy flow more slowly at the ion sound speed. To reach the target, energy flux from the midplane must pass through the sheath which limits heat flux to $q_{div} \approx 8\Gamma_i T_e$, where Γ_i is the ion flux at the target. To accommodate the increased ELM heat flux either the ion flux or T_e at the target must increase. In DIII-D the typical target particle flux before an ELM would imply the sheath could handle no more than 10% of the ELM heat flux, even if the divertor electron temperature rises to that of the pedestal. In this model T_e in the SOL would rise to that of the pedestal, limiting conduction from the pedestal, until the large ELM ion flux arrives at the target at the ion sound speed. In this scenario ELM conducted energy would then be set by the ratio of ion sound time, $L_{\|}/C_s$, to the duration of the ELM instability, τ_{ELM}.

Indirect evidence of the sheath's role in restricting parallel electron conduction during an ELM can be examined with DIII-D SOL and divertor diagnostics. The first indication that the sheath is limiting loss of electron thermal energy from the pedestal would be for T_e in the SOL to rise to a significant fraction of the pedestal T_e during an ELM. This is examined in the perturbation to the SOL T_e as plotted in Fig. 8. The profiles in this plot are produced in the same manner as those in Fig. 3, but extended into the SOL. The time dependence of the SOL Thomson scattering measurements that produced these profiles is shown in Fig. 9. Though there is a clear signal of a density rise in the SOL, the rise in T_e is less than 100 eV within 200–300 μs after an ELM. This low density discharge has pedestal parameters of $n_{e,ped} \sim 5\times10^{19}$ m^{-3}, or $n_{e,ped}/n_{GW} \sim 0.4$, and $T_{e,ped}$

~750 eV. These parameters correspond to an ion sound speed time from the outer midplane to the outer and inner targets of ~50 μs and ~120 μs respectively. The decay time of the SOL from $T_{e,ped}$ during an ELM would be expected to be of this same order if the sheath was limiting heat flow from the pedestal. Though there is no evidence from the Thomson data that the SOL T_e ever reaches $T_{e,ped}$, this can not yet be taken as definitive as it is barely within the time resolution of the analysis. Finally, other discharges where the Thomson laser fired either during, or <100 μs after, an ELM also exhibited a rise in SOL T_e of only a fraction of $T_{e,ped}$.

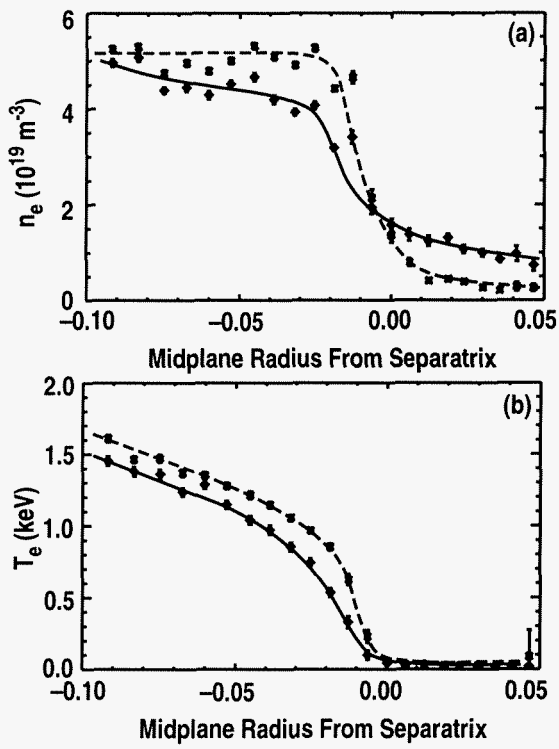

FIG. 8. Radial profile of the pedestal and SOL (a) n_e and (b) T_e just before and just after an ELM from Thomson scattering.

To further examine what role the sheath may be playing in parallel transport of energy during an ELM a number of pedestal and divertor diagnostics viewed the discharge of Fig. 9 with fast time resolution as shown in Fig. 10. The first indication of rapid parallel transport of electron energy is the fast drop in the pedestal SXR emission which is very sensitive to T_e. The SXR signal drop indicates a rapid perturbation to the pedestal T_e in ≤100 μs, the time resolution of the SXR diagnostic. The divertor D_α, J_{sat}

and heat flux, also shown in Fig. 10, indicate that the ELM pulse quickly travels to both divertors. The inboard and outboard divertor D_α signals rise together as does the ion saturation current measured by Langmuir probes in the divertor target. The resulting target heat flux, measured by IR emission, is of similar magnitude in both the inboard and outboard divertors. The slower rise and fall of the heat flux is due to the slower time response of the IR camera, ~100 μs, than the other particle flux diagnostics. There is ~100–200 μs ELM-to-ELM variability in the simultaneity of the ELM particle pulse to the inboard and outboard divertors. Further work will be required to detail propagation of ELM particles through the SOL.

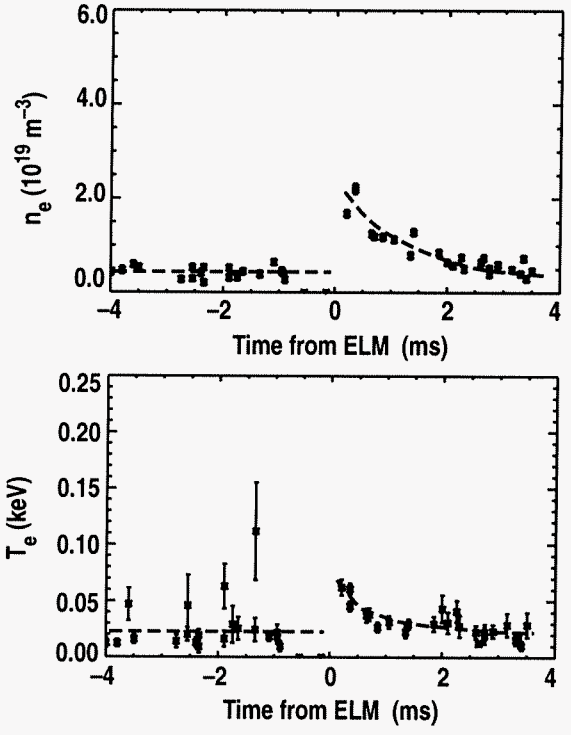

FIG. 9. The time dependence of (a) n_e and (b) T_e at 1 cm outside the separatrix mapped to the outer midplane. This data is the basis for the profiles of Fig. 8.

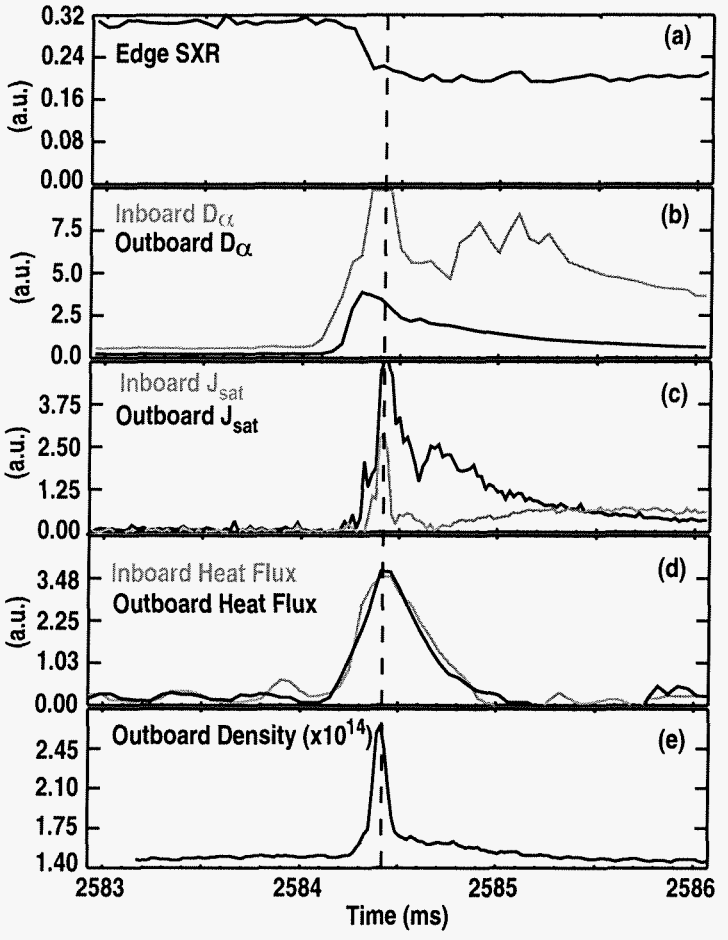

FIG. 10. Time behavior of ELM characteristics at low density. Shown are the pedestal SXR, inboard and outboard divertor D_α, inboard and outboard J_{sat} from Langmuir probes, the peak heat flux at the inboard and outboard divertor, and the interferometer signal passing through outboard divertor.

An indication of a process that might allow greater heat flux through the target sheath is shown in the last trace of Fig. 10. This trace is from a CO_2 interferometer which measures the line integral of density on a vertical path through the main plasma and outboard divertor. The line integral of the density along this path rises from a value of 1.4×10^{20} m^{-2} before the ELM to a peak value of $\geq1.8\times10^{20}$ m^{-2} in less than $\approx$100 μs during an ELM. We estimate the rise in divertor density at an ELM to be at least 2×10^{20} m^{-3} given the path length of 18 cm through the divertor and the assumption that the density does not rise in the main plasma during an ELM. The density rise could actually be significantly larger if it is localized near the divertor surface. With a pre-ELM divertor density of ~4×10^{19} m^{-3}, as measured by Thomson scattering, and a similar pedestal density, the rise in divertor density to a much higher level indicates local

generation of plasma at the target rather than pedestal ions flowing to the divertor. One possible source of particle generation is local ions falling through a raised sheath created by fast electron conduction from the pedestal. Each ion, accelerated to several hundred eV, or more, could dislodge several neutrals from the target allowing for a rapid buildup of density and particle flux. A related observation of density generation in the SOL due to ELMs has been made on JT-60U [21]. The increased particle flux from this process, and other factors such as secondary electron emission at the target, might increase the heat flux capacity of the sheath to a level that does not restrict energy transport from the pedestal into the SOL.

A critical issue for ELM energy transport in the SOL and divertor is determining the sheath characteristics during an ELM. Through the processes outlined above, a sheath potential as high as several hundred eV might produce sufficient heat flux capacity at the target yet not restrict electron conduction from the pedestal. In addition, even if the sheath does not limit energy transport from the pedestal it will still very likely affect other important ELM characteristics such as the spatial profile and deposition time of the ELM energy onto the vessel walls. Investigation of sheath effects during an ELM remains a high priority for future work.

There is also evidence of significant radial transport in the SOL during an ELM. This can be seen in the far SOL profiles of Fig. 8. The SOL density profile indicates a rise in density of $\sim 1\times10^{19}$ m^{-3} at 5 cm outside the separatrix at the midplane within several hundered μs after the onset of the ELM instability. The flat profile suggests the density perturbation likely extends another 2–3 cm, to the location of the outer midplane wall. This observation is also confirmed by fast microwave reflectometry measurements which measure a rise in density all the way to the outboard midplane limiter in ≤500 μs after an ELM. The decay time of the SOL density to the pre-ELM, Fig 9(a), state is 1–2 ms for both diagnostics. The integral of the rise in density around the plasma periphery is roughly equal to the density loss of the pedestal at each ELM. A density rise at the midplane might possibly be attributed to pedestal ions recycling off the target and then equilibrating around the SOL [22]. However the flow reversal of density from the divertor after an ELM would be expected to be slower, ≥1 ms after the ELM heat pulse

has been dissipated. No such slower rise in density has been observed in the midplane SOL.

The SOL density measurements at an ELM are important in that they indicate a significant fraction of the pedestal ions strike the main chamber walls instead of flowing into the divertor. An ion-electron equilibration time of ~400 μs at these parameters also implies such ions would carry much of their energy to the main chamber walls. While the density perturbation extends out to at least 5 cm outside the separatrix, the width of the divertor heat flux due to an ELM is measured to be only 1–2 cm mapped to the outer midplane, or 1–2 times the steady state heat flux width. These observations could be explained if electron conduction, not a flux of pedestal ions into the divertor, is responsible for the electron energy deposited on the target. The quantitative fraction of pedestal ions striking the main chamber and the poloidal and toroidal distribution of that flux is not yet known. Additional distributed measurements of ELM flux to the main chamber walls will be required to fully asses and characterize the radial ion transport at an ELM.

III. DISCUSSION

At high density the ELMs in DIII-D become smaller through a reduction in the conducted energy, while the convected energy remains constant. These small ELMs appear to be just within a tolerable range if scaled to a larger burning plasma tokamak such as ITER. It is important to understand the processes that lead to these small ELMs in order to adequately predict operation in a future devices. MHD analysis of these discharges suggest that smaller ELMs result from both a loss of edge bootstrap current at higher collisionality, and a narrower pedestal at high density. A burning plasma, even at high normalized density, will be expected to have a low collisionality pedestal to meet its confinement goals and this would suggest large ELMs. The pedestal width is also an important stability parameter, but its scaling to a larger tokamak is still uncertain [23]. Some recent work on DIII-D suggest the pedestal width may be set, at least in part, by the neutral fueling penetration depth [24]. This process would suggest a narrower pedestal width, and smaller ELMs for future large tokamaks. This might also offer some flexibility in setting the pedestal width to optimize a trade off between confinement and ELM size. Finally, though a successful correlation has been established between ELM size and edge stability, further advances are needed. Codes that can couple transport to nonlinear and nonideal evolution of the edge MHD modes would significantly improve predictive capability. They might also improve our understanding of convective transport.

The SOL and divertor measurements do not indicate that the sheath is playing a decisive role in setting the level of energy lost from the pedestal due to an ELM. However, previous measurements indicate the ELM heat flux deposition time is correlated with ion sound speed flow from the midplane to the divertor [18]. This would particularly be expected at high density where the transport of energy from the pedestal to the SOL is mostly convective. This should lead to longer deposition times and better compatibility for ELMs in the larger size off a burning plasma device. One final concern is the main chamber fluxes due to an ELM. Because of the longer ion equilibration times any ion lost from the pedestal will likely carry most of its energy to the wall or target. If a fraction of the ion flux is spread evenly about the main chamber this effect could be

beneficial. However if the flux is localized to a small area at the outer midplane damage to plasma facing components is possible. More work is needed to characterize this effect.

REFERENCES

[1]A. W. Leonard, A. Herrmann, K. Itami, *et al.*, J. Nucl. Mater. **266-269**, 109 (1999).

[2]G. Janeschitz, ITER JCT and HTs, J. Nucl. Mater. **290-293**, 1 (2001).

[3]J. L. Luxon, Nucl. Fusion **42**, 614 (2002).

[4]K. H. Burrell, M. E. Austin, D. P. Brennan, *et al.*, Plasma Phys. and Control. Fusion **44**, A253 (2002).

[5]Y. Kamada, Plasma Phys. Control. Fusion **42**, A247 (2000).

[6]J. Stober, M. Maraschek, G. D. Conway, *et al.*, Nucl Fusion **41**, 1123 (2001).

[7]M. Greenwald, R. Boivin, P. Bonoli, R. Budny, C. Fiore, J. Goetz, R. Granetz, A. Hubbard, I. Hutchinson, J. Irby, *et al.*, Phys. Plasmas **6,** 1943 (1999).

[8]D. A. Mossessian, P. B. snyder, M. Greenwald, J. W. Hughes, Y. Lin, A. Mazurenko, S. Medvedev, H. R. Wilson, and S. Wolfe, Plasma Phys. Control. Fusion **44**, 423 (2002).

[9]G. Federici, G. Janeschitz and A. Loarte, "Key Physics and Plasma-Material Interaction Issues of the ITER divertor and PFCs," in Proc. of the 15th Int. Conf. on Plasma Surface Interactions on Controlled Fusion Devices, Gifu, Japan, 2002, and to be published in J. Nucl. Mater.

[10]A. W. Leonard, J. A. Boedo, M. E. Fenstermacher, et al., "Transport of ELM Energy and Particles Into the SOL and Divertor of DIII-D," in Proc. of the 15th Int. Conf. on Plasma Surface Interactions on Controlled Fusion Devices, Gifu, Japan, 2002, and to be published in J. Nucl. Mater.

[11]A. Loarte, M. Becoulet, G. Saibene, et al., Plasma Phys. Cont. Fusion 44, 1815 (2002).

[12]A. Loarte, G. Saibene, R. Sartori, et al., " ELM Energy and Particle Losses in Present Tokamaks and their Extrapolation to Burning Plasma Experiments" in Proc. of the 15th Int. Conf. on Plasma Surface Interactions on Controlled Fusion Devices, Gifu, Japan, 2002, and to be published in J. Nucl. Mater.

[13]A. W. Leonard, R. J. Groebner, M. A. Mahdavi, et al., Plasma Phys. and Control. Fusion **44**, 945 (2002).

[14]J. W. Connor R. J. Hastie and H. R. Wilson, Phys. Plasmas **5**, 2687 (1998).

[15]P. B. Snyder, H. R. Wilson, J. R. Ferron, *et al.*, Phys. Plasmas **9**, 2037 (2002).

[16]O. Sauter, C. Angioni, and Y. R. Lin-Liu, Phys. Plasmas **6**, 2834 (1999).

[17]D. M. Thomas "Poloidal Magnetic Field Measurements and Analysis With the DIII-D LIBEAM System," in Proc. of the 14th Topical Conf. on High-Temperature Plasma Diagnostics, Madison, Wisconsin, 2002, to be published in Rev. Sci. Instrum.

[18]A. V. Chankin, N. Asakura, T. Fukuda, *et al.*, Nucl. Fusion **42**, 733 (2002).

[19]A. Herrmann, P. Andrew, T. Eich, *et al.*, "Stationary and transient divertor heat flux profiles and extrapolation to ITER," in Proc. of the 15th Int. Conf. on Plasma Surface Interactions on Controlled Fusion Devices, Gifu, Japan, 2002, accepted for publication in J. Nucl. Mater.

[20]A. Bergmann, Nucl. Fusion 42, 1162 (2002).

[21]A. Chankin, N. Asakura, T. Fukuda, *et al.*, "Influence of Plasma-Wall Interactions on the Behavior of ELMs in JT-60U," in Proc. of the 15th Int. Conf. on Plasma Surface Interactions on Controlled Fusion Devices, Gifu, Japan, 2002, and to be published in J. Nucl. Mater.

[22]ITER Physics Basis Editors, ITER Physics Expert Group Chairs and Co-Chairs and ITER Joint Central Team and Physics Integration Unit, Nucl. Fusion **39**, 2442 (1999).

[23]T. H. Osborne, J. G. Cordey, R. J. Groebner, *et al.*, "Characteristics of the H–Mode Pedestal and Extrapolation to ITER," in Proc. of the 19th Fusion Energy Conf., Lyon, France, 2002 (International Atomic Energy Agency, Vienna, 2002) to be published on CD-ROM.

[24]R. J. Groebner, M. A. Mahdavi, A. W. Leonard, *et al.*, "Correlation of H-mode Barrier Width and Neutral Penetration Length," in Proc. of the 19th Fusion Energy Conf., Lyon, France, 2002 (International Atomic Energy Agency, Vienna, 2002) to be published on CD-ROM.

ACKNOWLEDGMENTS

This is a report of work supported by the U.S. Department of Energy under Contracts DE-AC03-99ER54463, W-7405-ENG-48, and DE-AC04-94AL85000 and Grant No. DE-FG03-01ER54615.